

Peacock: A Persistent Wide-Field-Of-View Simultaneous Multispectral System Based on COTS Hardware

Tamara E. Payne, Philip Castro, Luke Weisenbach

Applied Optimization Inc.

Ethan VanTilburg, Matthew Wilson

Applied Optimization Inc.

Trenton Godar, Veronica Wiley

U.S. Government

James Frith, Scott P. Milster

AFRL/RVSW

ABSTRACT

We present Applied Optimization's (AO) new custom telescope system called Peacock. Peacock is a persistent, wide-field-of-view, simultaneous, multispectral system based on Commercial Off the Shelf (COTS) hardware. Peacock uses a set of four identical telescope systems boresighted together via a custom holder on a Paramount MEII mount, each with a different astronomical filter (Sloan g' , r' , i' , and z') with four identical CCD detectors. The system was designed, assembled, and is operated by Applied Optimization. The system allows simultaneous, four-filter photometry for satellite characterization in support of Space Domain Awareness (SDA).

We discuss the motivation for building this system, the hardware engineering involved, the system control software, and the photometric and astrometric processing pipeline. The system is controlled using in-house software to control each telescope system for synchronization. The photometric and astrometric processing pipeline uses in-house software to reduce the observations, extract the flux of the resident space objects, and calibrate the photometry onto a standard photometric system.

We present the initial results of the system generating persistent signatures of multiple Geosynchronous Earth Orbit satellites (GEOs) within a single FOV: multi-spectral signatures, color-index signatures, and color-color plots. We describe the photometric errors of the current system using in-frame photometric calibrations and future work to implement improvements planned for future data products. We discuss the utility of persistent, simultaneous, multi-spectral signatures for SDA.

1.0 INTRODUCTION

In a space warfighting environment that is congested, competitive, and contested, it is vital that timely, high-fidelity monitoring, change detection, and characterization of objects in Deep Space, particularly the Geosynchronous Earth Orbit (GEO) belt, be performed. The most effective approach for enhancing our current capabilities is to do more with the wide field of view (WFOV), staring sensors that currently collect all-night, panchromatic observations on objects in and near the geosynchronous belt that produces high cadence and long duration photometric and astrometric data. Duration and data cadence are critical factors that need to be optimized in order to properly sample objects that are dynamic in either orbit or attitude control or both. Formerly quiescent three-axis stabilized objects are now actively changing their attitude profile in order to execute their missions. Both hazard and threat objects will be dynamic by definition. Therefore, we have leveraged the current Commercial Off the Shelf (COTS) camera WFOV technology to improve Signal to Noise Ratio (SNR), maintain astrometric accuracy and precision, persistence, and coverage, and improve photometric accuracy and precision.

The new system, called Peacock, is a set of four COTS camera systems boresighted together, each with a different spectral filter in the Sloan Gen 2 photometric system. Peacock collects simultaneous photometry in four filters that enable higher accuracy color analysis of dynamic objects heretofore impossible to accomplish. See Fig. 1. Why simultaneous multi-spectra filter photometry is more accurate is presented in [1]. We have demonstrated a proof-of-concept system that will cover approximately four degrees of the GEO belt. The compact and modest cost of each quadrature telescope means that it can be replicated cost-effectively to cover the entire GEO belt and deployed at a

ground site. Each quad telescope is oriented to different but overlapping regions of the GEO belt to accomplish full GEO belt coverage over the site. For a mid-latitude site, twelve such telescopes in an array configuration would be required for complete GEO belt coverage above 30 degrees elevation.



Fig. 1. Peacock telescope at John Bryan Observatory, Yellow Springs, OH

Peacock is not the first simultaneous multi-spectral system. Tanner Campbell reported on how to characterize Low Earth Orbit objects using a simultaneous multi-color optical array [2]. The differences between Peacock and Campbell's system (at least at the time of his reporting) are: 1) a smaller FOV than Peacock, 2) no single control over all four cameras.

2.0 METHODS AND PROCEDURES

The hardware and software are a combination of Applied Optimization (AO) custom and Commercial Off The Shelf (COTS) technology.

2.1 Hardware

Each optical system is a Takahashi FSQ106-EDX with a COTS filter holder by Baader for each of the COTS Sloan filters made by Astrodon (now Optical Structures Inc.) with a Finger Lakes Instrumentation MicroLine16803 Charge-Coupled Device (CCD) to collect the spectral images. A custom adapter was designed by AO to secure the CCD to the filter folder. We used a COTS mount by Software Bisque so that Peacock would have a tracking capability as well as persistent staring mode with tracking off for GEO observations. The tracking capability added functionality for tracking non-GEO objects including stars.

AO designed a custom telescope holder and accompanying counterweights for the Declination axis and the Right Ascension axis of the mount. A custom adapter plate connects the telescope holder to the MEII mount. Each optical system has an AO-custom tip-tilt stage to enable alignment and pointing to within 17.5 arcseconds (5 pixels).

The Takahashi FSQ-106EDX4 is a double extra-low dispersion Quadruplet refractor with an edge-to-edge $3.97^\circ \times 3.97^\circ$ FOV. The ML16803 has fast download speeds that maintain a 16-bit resolution. It uses a USB 2.0 interface to communicate with the Peacock's control system. The Software Bisque Paramount MEII is a German equatorial mount with negligible backlash and high pointing and tracking accuracy.

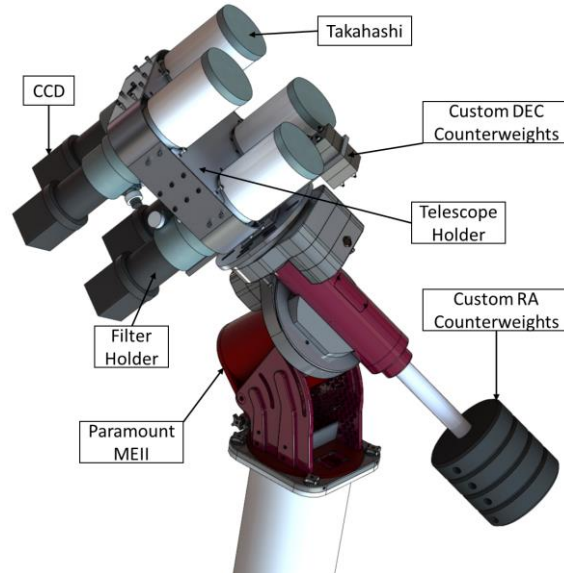


Fig. 2. Hardware comprising the Peacock telescope using both custom and COTS hardware

2.2 Control Software

The control software is also a combination of AO custom and COTS technology. The control of the mount is performed with Software Bisque's TheSkyX software. The control and synchronization of the cameras is performed with the AO-custom software. The shutter synchronization is consistently better than 3 milliseconds. The control software takes advantage of TheSkyX's capability to receive scripted commands via its Transmission Control Protocol (TCP) server and utilizes FLI's Software Development Kit (SDK) for image capture.

AO's custom control software, Pyhen – a combination of **Python** and **Peahen**, a female Peacock, is a Python module to control the Peacock telescope. Pyhen solves the problem of synchronizing four camera shutters, and collecting and storing Flexible Image Transport System (FITS) files from the four cameras simultaneously. While some programs on the market (such as TheSkyX) can handle multiple CCDs simultaneously, the camera selection is typically limited to a single primary sensor CCD and a separate CCD for guiding.

Features of Pyhen include:

- Control of a telescope mount using TheSkyX
- Control of an arbitrary number of cameras using FLI's SDK
- Boresighting tools to align multiple cameras to within pointing accuracy requirements
- Automatic data compression and storage using the bzip2 algorithm
- Fully parallelized to maximize data throughput
- Written as a Python module to be easily integrated into other programs
- It can be easily modified to allow for control of other sensor types

2.3 Multi-spectral Image Processing Software (MIPS)

With a persistent, staring sensor, a large quantity of raw image data is collected every night. Care should be taken to both collect and store the data in a way that is easily manageable and maintainable for the future, which includes filenames, folder structure and naming conventions, along with data compression.

MIPS is AO's custom image processing software to reduce the raw images, extract the photometry from the reduced images, calibrate the photometry by removing atmospheric effects, transform the instrumental magnitudes to a standard photometric system, i.e., generate exo-atmospheric magnitudes [3][4], and archive the data and metadata of the collection in the standard Electro-Optical Space Situational Awareness (EOSSA) format [5] [6]. See [7] for the authors' previous paper related to generating precision values for the resulting photometry.

In-frame calibrations were added to MIPS functionality in order to take advantage of the large FOV and to eliminate the need to step off the target field and take observations of photometric standard stars. It is also the hope that in-frame calibrations will provide better transformations to the standard photometric system than all-sky calibrations under non-ideal observing conditions (e.g., partial cloudy skies).

In-frame calibrations are implemented using the APASS DR10 catalog as the photometric standard star catalog and performed by calculating the average of the difference between the catalog magnitude and the instrumental magnitude of the streaking stars in the FOV. The difference between the catalog magnitude and the instrumental magnitude consists of the sum of the zero-point and the first-order extinction coefficient, assuming the color term and second-order extinction coefficient are zero. The error of the standard (exo-atmospheric) magnitude is calculated by combining the error of the instrumental magnitude and the in-frame calibration error in quadrature.

3.0 RESULTS

We present the first light image from Peacock, persistent signatures of seven GEOs that are in a single FOV of the system collected during one photometric night in June 2022, and discuss the photometric errors of the system to date.

3.1 First Light

First light was January 9, 2021 when we observed the Orion Nebula. Using the simultaneous four spectral filters, we formed a composite color image of the nebula based on scaled brightnesses through the Sloan filters. See Fig. 3.



Fig. 3. Orion Nebula (M42/NGC 1976) composite color image from Sloan Gen 2 filter system with four filters (g'r'i'z')

3.2 Persistent GEO Signatures

A region of the GEO belt visible from the John Bryan Observatory (JBO) in Ohio contains the 101° – 103° clusters on UTC 2022-06-18. An image of this field taken with Peacock is shown in Fig. 4. The field is 3.97 degrees by 3.97 degrees (4096 pixels x 4096 pixels). The 101 cluster is on the right and the 103 cluster is on the left. Note the star streaks showing the system is not sidereal tracking, but persistently staring at this field. Also note there are some non-GEO objects in the FOV along with at least one highly inclined GEO that were not processed.

We present multi-spectral signatures for seven satellites in this field: 3 in the 101 cluster and 4 in the 103 cluster. Note in Fig. 4 that 4 satellites appear in the 101 cluster on the right, but one has a highly inclined orbit and was not included in this analysis. The information on these satellites is listed in Table 1. Note that there are three pairs of identical or similar satellites. The first pair is DirecTV 10 and 12 with identical bus and payloads launched 2 years apart. The second pair is SES 1 and 3 that have the same bus, but there are differences in the payloads. They were launched 1 year apart. The third pair is DirecTV 15 and AT&T T-16, which were launched 4 years apart and have slight differences in their buses and payloads [8].



Fig. 4. Peacock image containing GEO clusters at longitudes 101° (right) and 103° (left)

Table 1. List of satellites and their properties

Satellite Name	Satellite ID	Bus Type	Launch Date	Comments
DirecTV 9S	29494	SSL-1300	13 Oct 2006	
DirecTV 10	31862	BSS-702	07 Jul 2007	
DirecTV 12	36131	BSS-702	29 Dec 2009	Same as DTV 10
SES 1	36516	Orbital Star-2.4	24 Apr 2010	
SES 3	37748	Orbital Star-2.4	15 Jul 2011	Similar to SES 1
DirecTV 15	40663	Eurostar-3000	27 May 2015	
AT&T T-16	44333	Eurostar-3000 LX Hybrid	20 Jun 2019	Similar to DTV 15

Fig. 5 shows the artist-conception drawings of each satellite [8]. Note that they are all communication satellites and so have two solar panel arrays and various types of transponders and antennas as their payloads. The figure is stacked so that similar satellite pairs are on each row as per Table 1.



Fig. 5. Artist conception of satellite configurations for the seven satellites we observed [8]

3.2.1 Multi-spectral Signatures

The persistent signatures of the satellites shown in Fig. 5 are presented in Fig. 6 – Fig. 9. The brightness of the satellite in each filter is plotted in units of exo-atmospheric magnitude with different symbols and colors for each filter along with the error bars showing the error in the exo-atmospheric magnitude of each data point. The brightnesses are plotted as a function of Longitudinal Phase Angle (LPA) in degrees (the east-west component of the total solar phase angle) with time increasing from left to right (from beginning to end of the night). Note that because these observations were taken from a mid-latitude, Northern hemisphere site near the Summer Solstice, the length of the night is short (about 5 hours long). There are spurious points mostly below, but sometimes above, the

bulk of the signature. These are caused by star streak contamination (in either the background annulus or the synthetic aperture) or one or two bad stars in the field. Future improvements to MIPS to exclude these data points is discussed in Section 4.0.

The plots are organized so that similar pairs of satellites are in the same figure. Note that in all seven cases, the satellites are faintest in the g' band and usually, but not always brightest in the z' band. Sometimes, the satellites are as bright in the i' band as the z' band.

Note the details of the solar panel peak of DirecTV 9S at about -12 degrees LPA present in Fig. 6. Instead of a single broad peak, two separate narrower peaks are detected. Also note that at around +5 degrees LPA, there are increases and decreases in brightness in the z' band that are not as prominent in the other bands. The double peak is more easily seen subsequently where a figure shows each filter separately (Fig. 10).

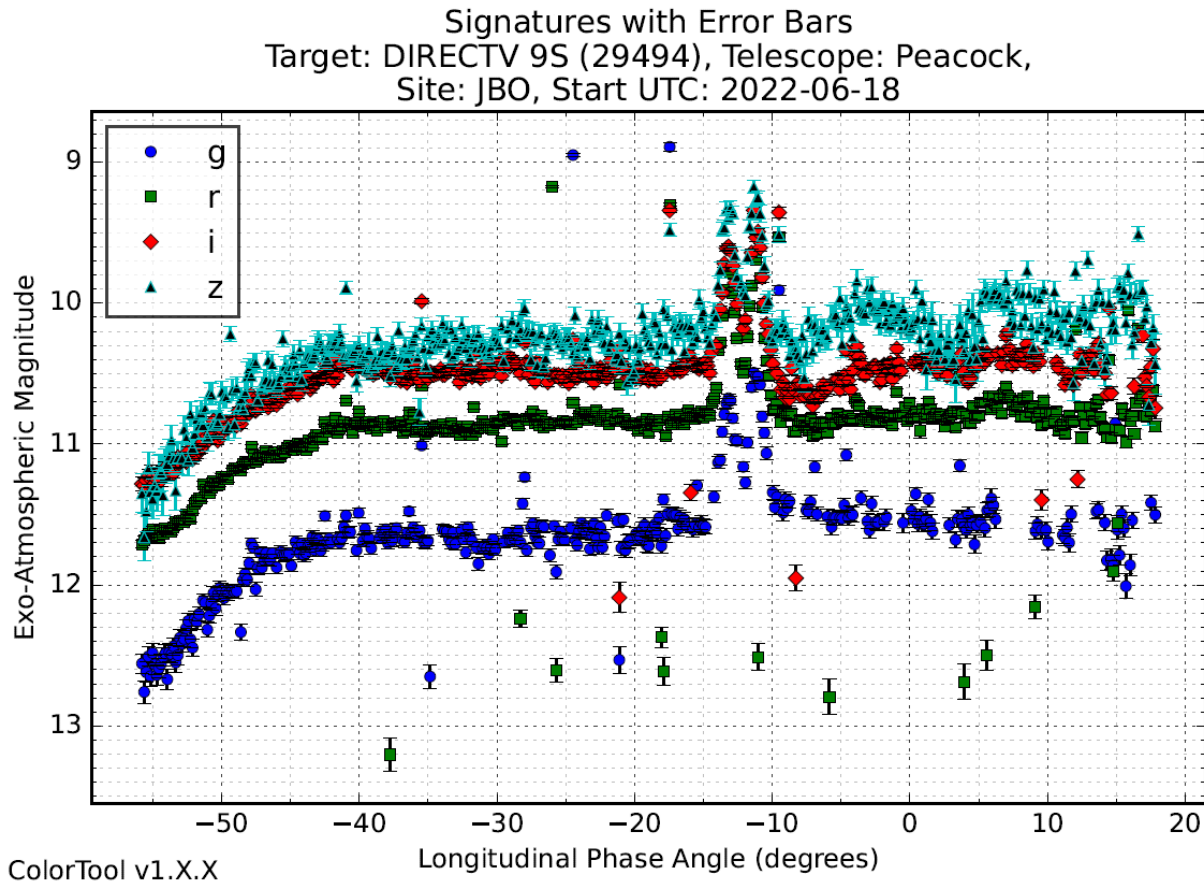


Fig. 6. $g'r'i'z'$ simultaneous signatures of DirecTV 9S (29494) taken on UTC 2022-06-18

The signatures of the Boeing BSS-702 bus satellites in Fig. 7 show no major peaks that we would attribute to solar panels, which indicates that the panels' glint angle did not pass over the observing site. There is a gradual, uniform increase in brightness that continues all night long until astronomical dawn. Note the similarities in the two signatures. Since they have the same satellite configuration and were launched only two years apart, we expect the multi-spectral signatures to be nearly identical. With persistent observations, a lot of smaller structure is present in the signatures that could be exploited for space object characterization and other SDA purposes. We know these minor undulations to be real because the night was photometric and therefore these variations are not due to clouds. Also note that for single exposures with a 4-inch telescope, the photometry has less precision than our goal of 0.05 mag or less for magnitudes fainter than about 12.5. We discuss this further in 3.3 and Section 4.0.

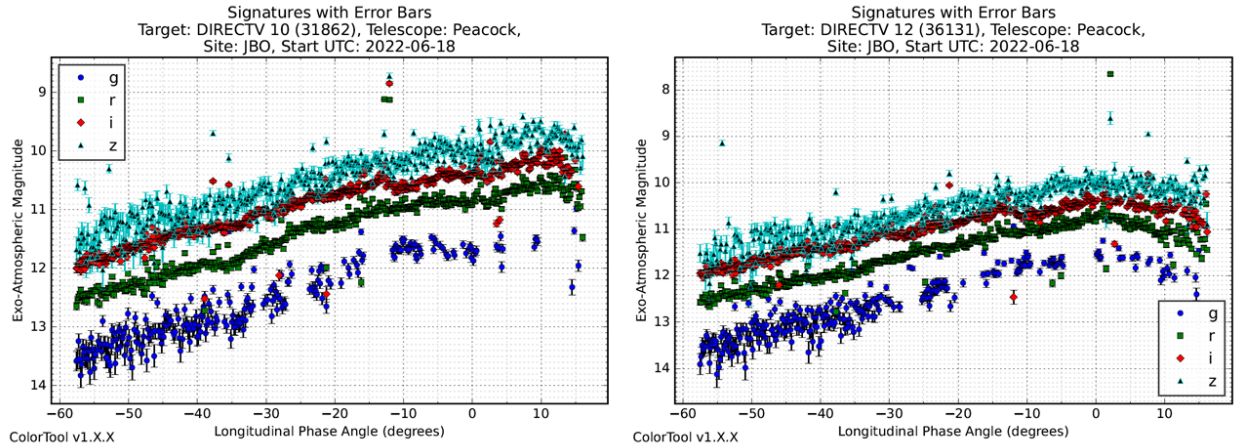


Fig. 7. g'r'i'z' simultaneous signatures of DirecTV 10 (31862) and DirecTV 12 (36131) taken on UTC 2022-06-18

Fig. 8 shows the signatures for SES 1 and 3. The signatures are very similar, which is expected since the satellites have similar configurations and were launched only one year apart. Note that both show a single, sharp solar panel glint, but offset from one another where SES 1's glint is at -23 degrees LPA and SES 3's glint is at -28 degrees LPA. However, the wings of the solar panel peaks are slightly different, where the wings are broader for SES 3. Both signatures have fairly smooth increases in brightness on the west side of the satellite (negative LPAs), but SES 3 has small undulations around -40 degrees LPA whereas SES 1 is smooth. This difference could be due to differences in the body or the payloads on the west side of the bus. Also note there are rapid variations in brightness in the z' band at around -5 degrees LPA for both satellites and similar variations in the i' band for SES 1 at the same LPA. It appears the signature is getting brighter again just before dawn, which indicates the signatures may mirror themselves in the positive LPA range. Observations during the winter when the night is longer (or a more westerly-located sensor) would capture the positive LPA range to verify this supposition.

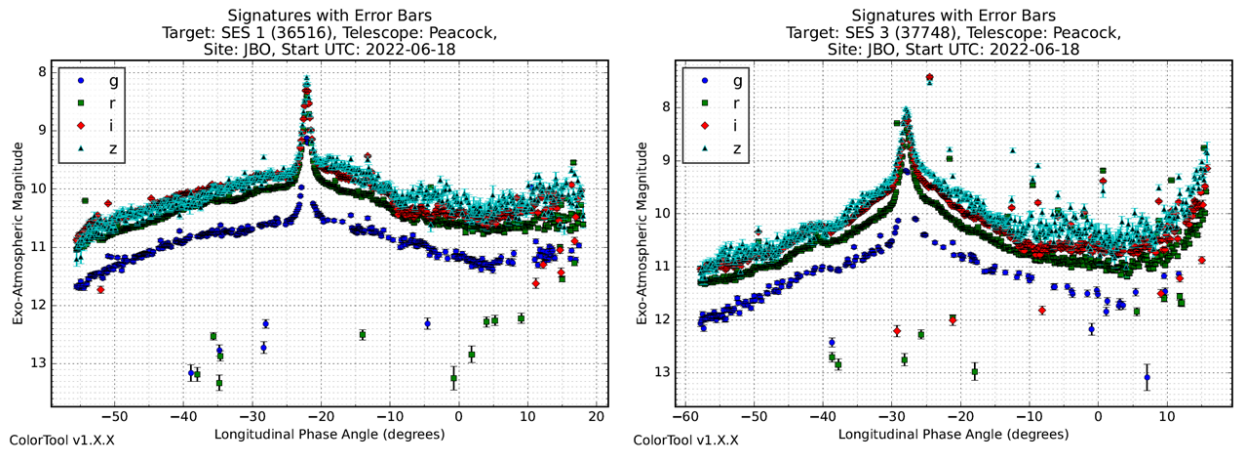


Fig. 8. g'r'i'z' simultaneous signatures of SES 1 (36516) and SES 3 (37748) taken on UTC 2022-06-18

The signatures for the Eurostar-3000 satellites are the smoothest, showing little to no rapid variations although there are some undulations in their brightnesses at around -10 degrees LPA as can be seen in Fig. 9. There is a similar dip in the signatures at approximately +5 degrees LPA. Again, the signatures are similar to one another since their configurations are very similar.

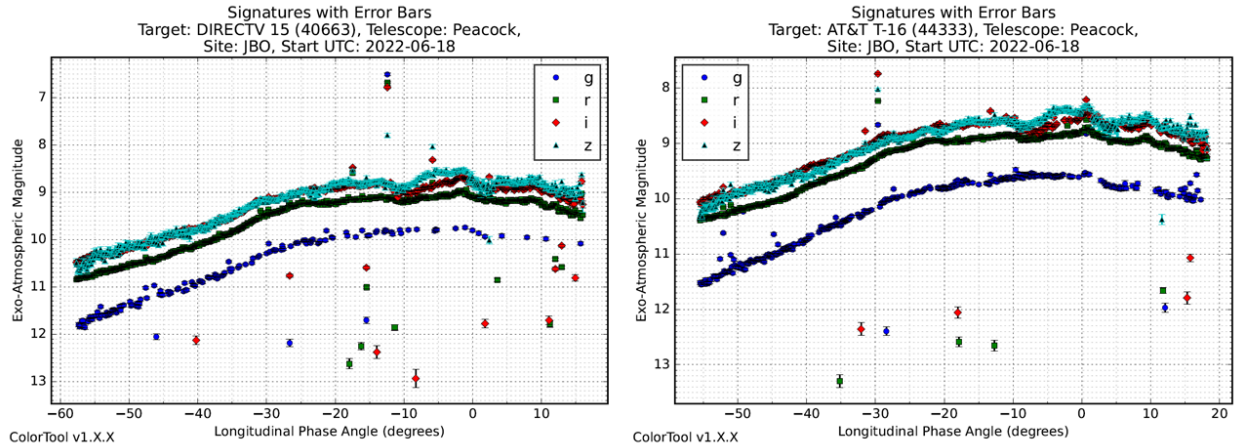


Fig. 9. g'r'i'z' simultaneous signatures of DirecTV 15 (40663) and AT&T T-16 (44333) taken on UTC 2022-06-18

To more closely examine details in the persistent, multi-spectral signatures, Fig. 10, Fig. 11, and Fig. 12 show the signatures through each filter separately. Satellites DirecTV 9S, SES 1, and AT&T T-16 (respectively) were chosen to highlight some of the finer details in the different types of signatures.

The double peak feature of the solar panels on DirecTV 9S can be clearly seen in Fig. 10 in all filters except for z'. Note the 0.5 magnitude slow undulation of the signature in z' starting at -5 degrees LPA.

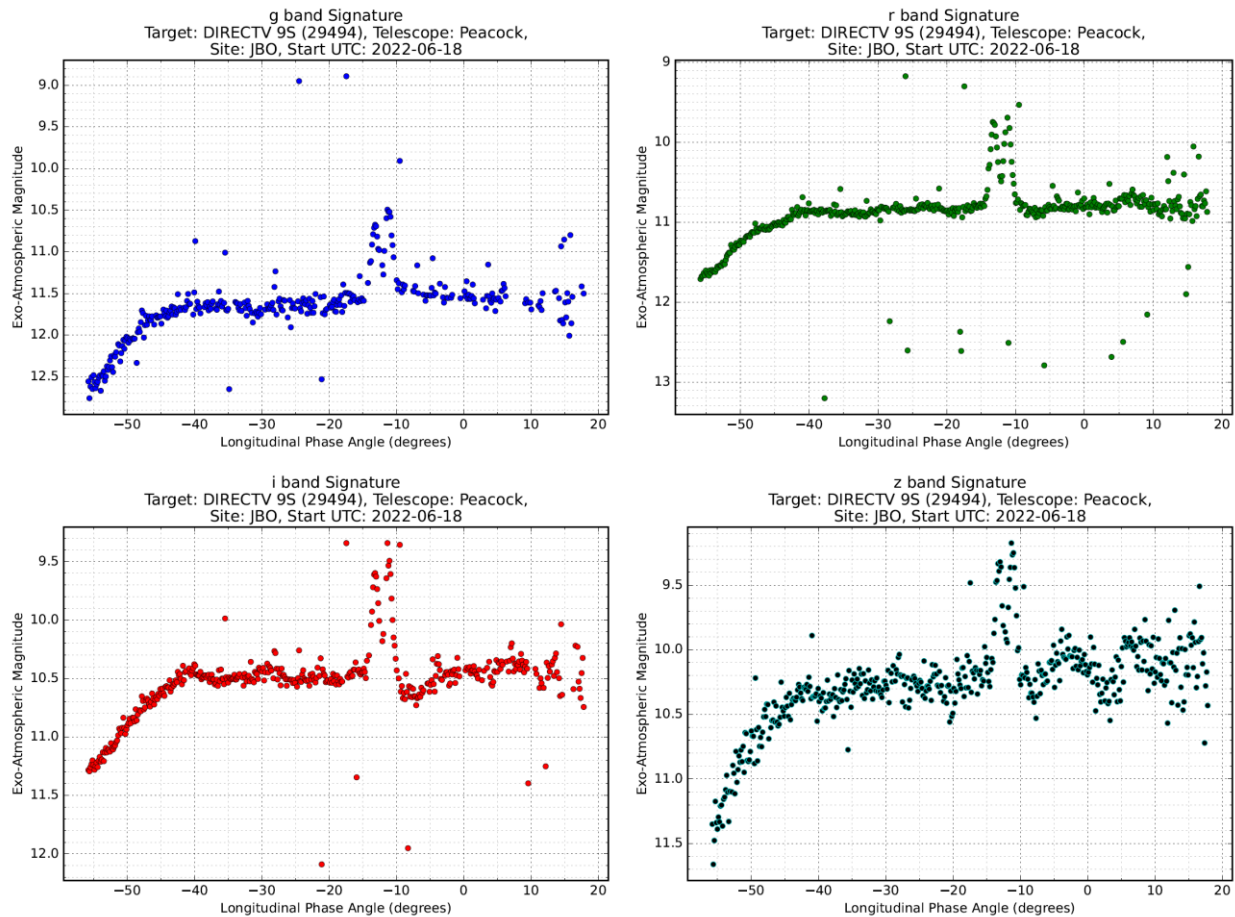


Fig. 10. Individual spectral filter signatures for DirecTV 9S (29494)

In Fig. 11, the single peak solar panel of SES 1 can be seen. Again, note the slow undulation in the z' signature starting at -10 degrees LPA and that there is a corresponding abrupt brightness shift at that same time in the i' signature.

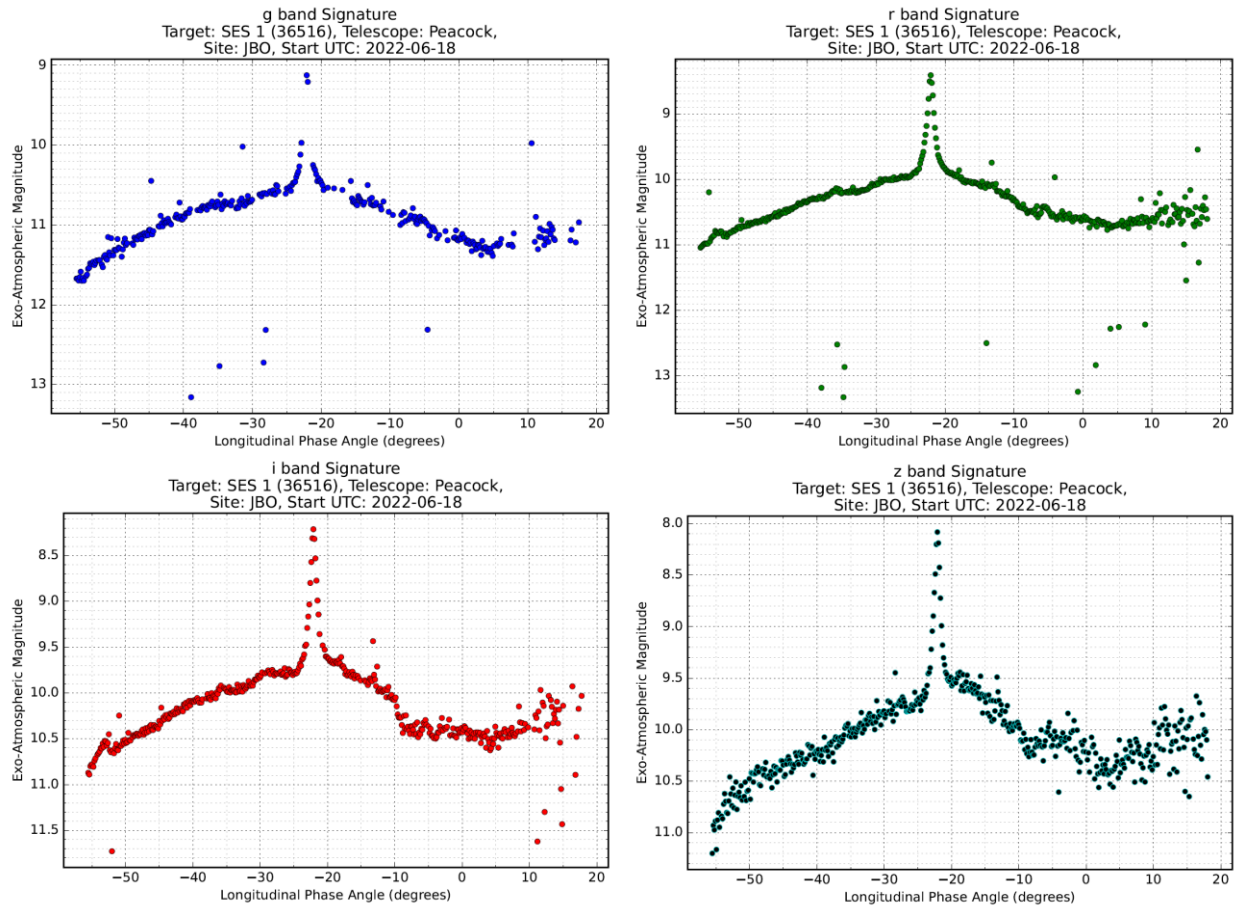


Fig. 11. Individual spectral filter signatures for SES 1 (36516)

Finally, Fig. 12 shows the spectral signatures of AT&T T-16, which do not display a bright solar panel glint at the LPAs it was observed. Note the smooth nature of all the signatures except in the z' band where there are undulations in the brightness starting at -25 degrees LPA until the end of the observations at astronomical dawn. Also note the small, short duration peak in brightness in all bands at +2 degrees LPA.

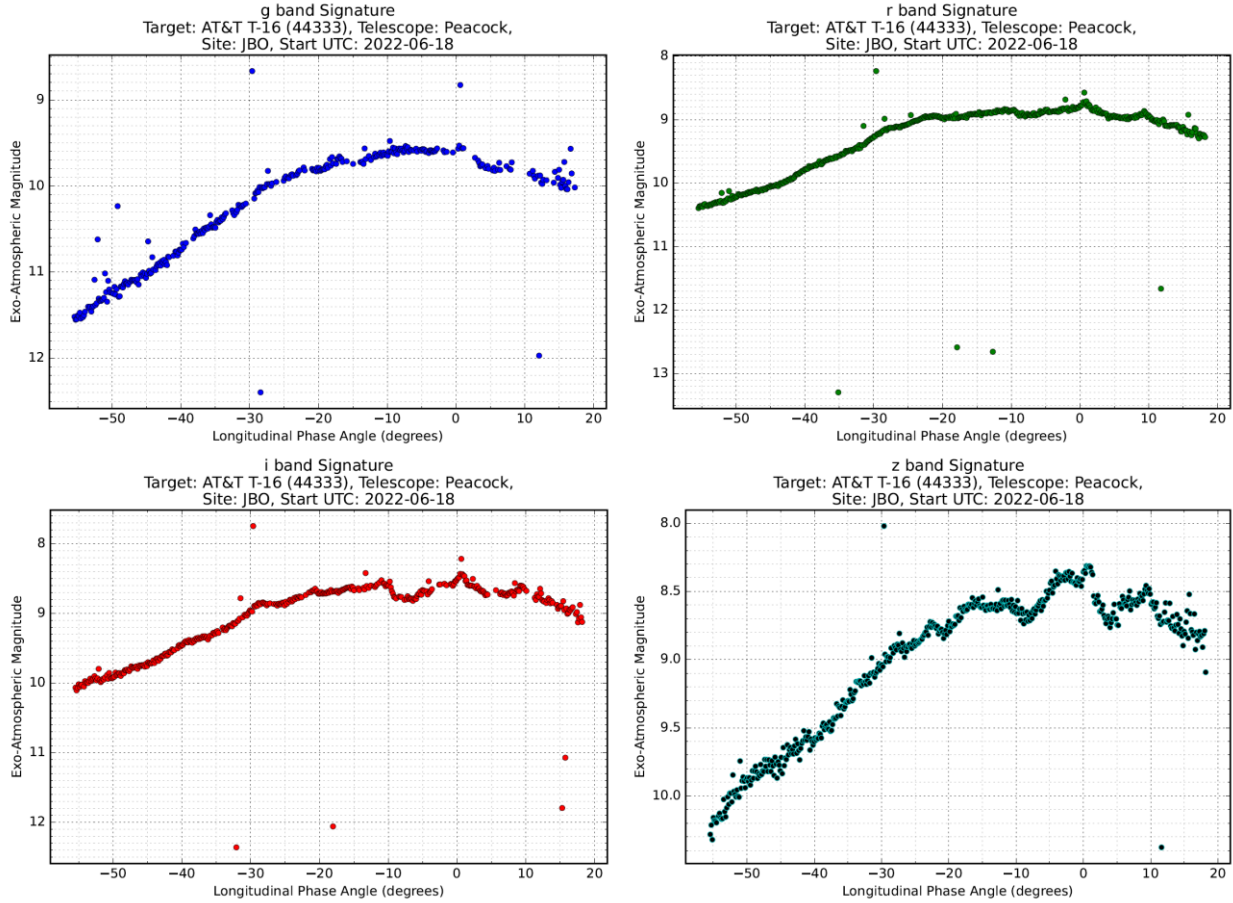


Fig. 12. Individual spectral filter signatures for AT&T T-16 (44333)

3.2.2 Color Analysis

To analyze the color of each satellite and how that color changes with time, we form color index signatures (a color index as a function of LPA). With four filters, there are six unique color indices formed via the equation:

$$m_1 - m_2 = -2.5 \log \frac{f_1}{f_2}$$

Where m_1 is the magnitude in one filter and m_2 is the magnitude in a second filter and the f 's are the corresponding fluxes through each filter. The convention is for m_1 to be at shorter wavelengths than m_2 , such that the larger the numerical value of a color index, the redder the object is. Recall that smaller numerical values for magnitudes means brighter or an increase in flux.

We have selected a color index that shows the most interesting features for a satellite. In the interest of space, we will focus on the three satellites already featured in this analysis: DirecTV 9S, SES 1, and AT&T T-16. Each color index can yield information about the satellite and furthermore, color index pairs can be used for Machine Learning cluster analysis techniques to exploit the spectrally diverse data further. So, a color-color plot is shown in conjunction with a color index signature for each satellite. The value of a color-color plot is that similar satellites reside in similar regions of the plot whereas different satellites reside in different regions of the plot. Note that the photometric outliers seen in the figures in Section 3.2.1 are present in the color index signatures and the color-color plots.

The $r'-i'$ color index signature for DirecTV 9S in Fig. 13 (left) shows that there is very little color difference over all the illumination angles sampled during this night near Summer Solstice, but there are small-scale fine color variations on short timescales that are intriguing and deserve further study. Even though we saw the double peaked solar panel glint, there is virtually no change in magnitude in this color index or any other. On the right in Fig. 13, the $r'-z'$ color index is plotted against the $g'-i'$ color index showing the main region in color-color space where this SSL-1300 bus type resides ($g' - i' = 1.2$ and $r' - z' = 0.6$).

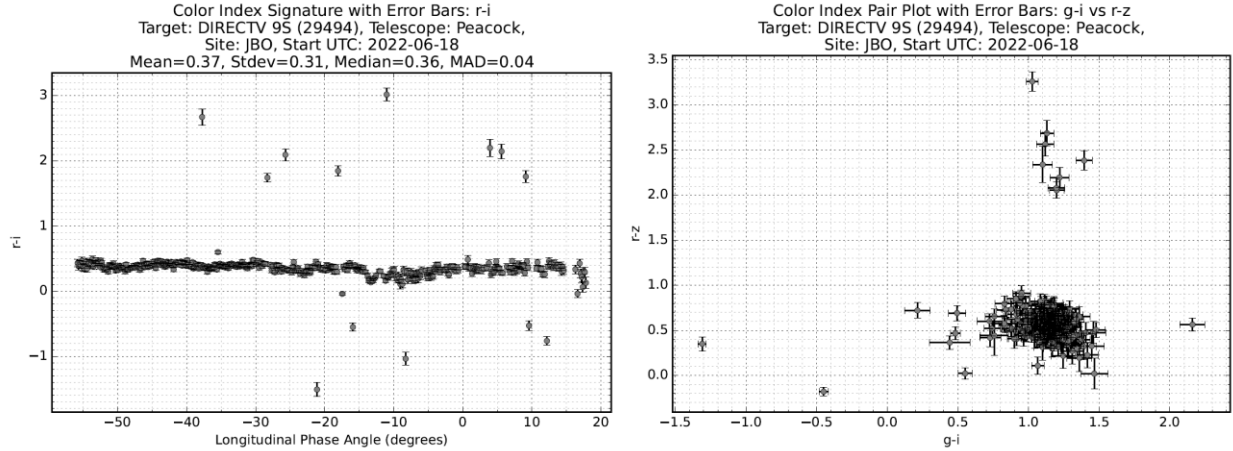


Fig. 13. $r'-i'$ color index signature (left) and $g'-i'$ vs. $r'-z'$ color-color plot (right) for DirecTV 9S (29494)

For SES 1, the $r'-i'$ signature also has very little variability throughout the night as shown in the left plot in Fig. 14, even during the time of its solar panel peak. On the right, the color-color region for SES 1 is $g' - i' = 0.8$ and $r' - z' = 0.3$. Comparing these colors with DirecTV 9S, SES 1 is bluer than DirecTV 9S in both color indices. For comparison, $g' - i' = 0.8$ and $r' - z' = 0.4$ for SES 3 (37748), which shares the Orbital Star-2.4 bus.

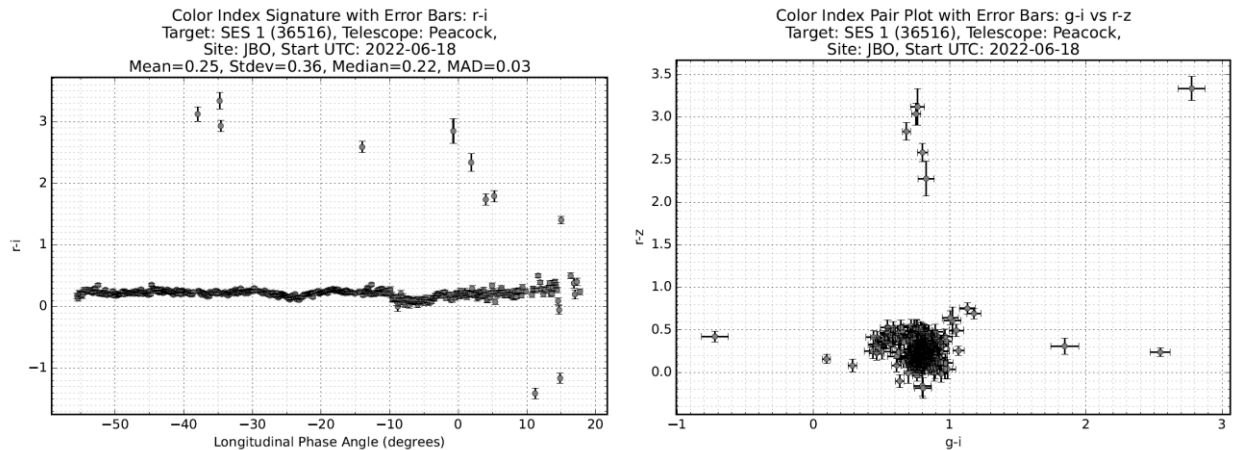


Fig. 14. $r'-i'$ color index signature (left) and $g'-i'$ vs. $r'-z'$ color-color plot (right) for SES 1 (36516)

Similarly for AT&T T-16, the left plot in Fig. 15 shows the $r'-i'$ color index to be approximately constant throughout the night. Recall that this signature contains no discernable solar panel peak. This Eurostar-3000 bus type resides in color-color region of $g' - i' = 1.2$ and $r' - z' = 0.3$, which is redder than SES 1, the same as DirecTV 9S in $g'-i'$. In $r'-z'$, it is the same color as SES 1, but bluer than DirecTV 9S. For comparison, $g' - i' = 1.2$ and $r' - z' = 0.3$ for DirecTV 15 (40663), which shares the Eurostar-3000 bus.

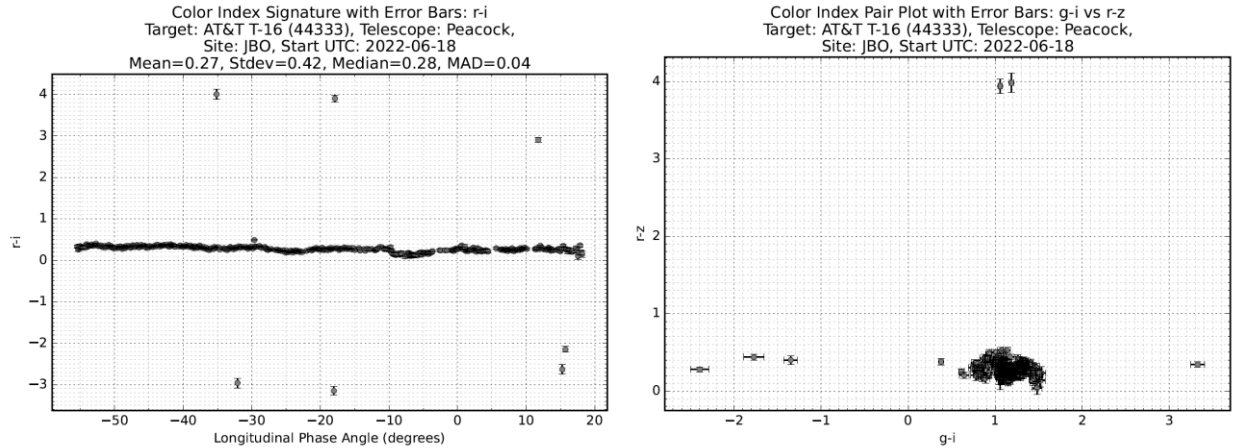


Fig. 15. $r'-i'$ color index signature (left) and $g'-i'$ vs. $r'-z'$ color-color plot (right) for AT&T T-16 (44333)

3.3 Photometric Error Analysis

As discussed in Section 2.3, MIPS is undergoing improvements including addressing the issues with bad stars, which causes clusters of outliers with larger magnitude errors as seen in the figures in Section 3.2. Similar to those signature figures, we present the photometric error of each exo-atmospheric magnitude as a function of LPA. We have chosen the same three satellites to illustrate the current state of our processing pipeline with respect to photometric error: DirecTV 9S, SES 1, and AT&T T-16. Our goal is for the error in exo-atmospheric magnitude to be no larger than 0.05. Recall that both measurement precision of the instrumental magnitude and magnitude errors in the photometric standard star catalog contribute to the overall exo-atmospheric magnitude error. The latter source of error should usually be much smaller than instrumental magnitude precision errors, but catalog errors should not be neglected.

The effect of frames with one or two bad stars can be seen Fig. 16 in the z' band from 0 - +5 degrees LPA for DirecTV 9S where the errors are as high as 0.15 mag. Note that the magnitude error is largest for z' and smallest for r' band ranging from 0.01 to 0.04 mag. The i' has the next smallest error and g' errors are larger than i' errors but smaller than z' errors. There is an exception at -8 degrees LPA where the i' error roughly matches the g' error.

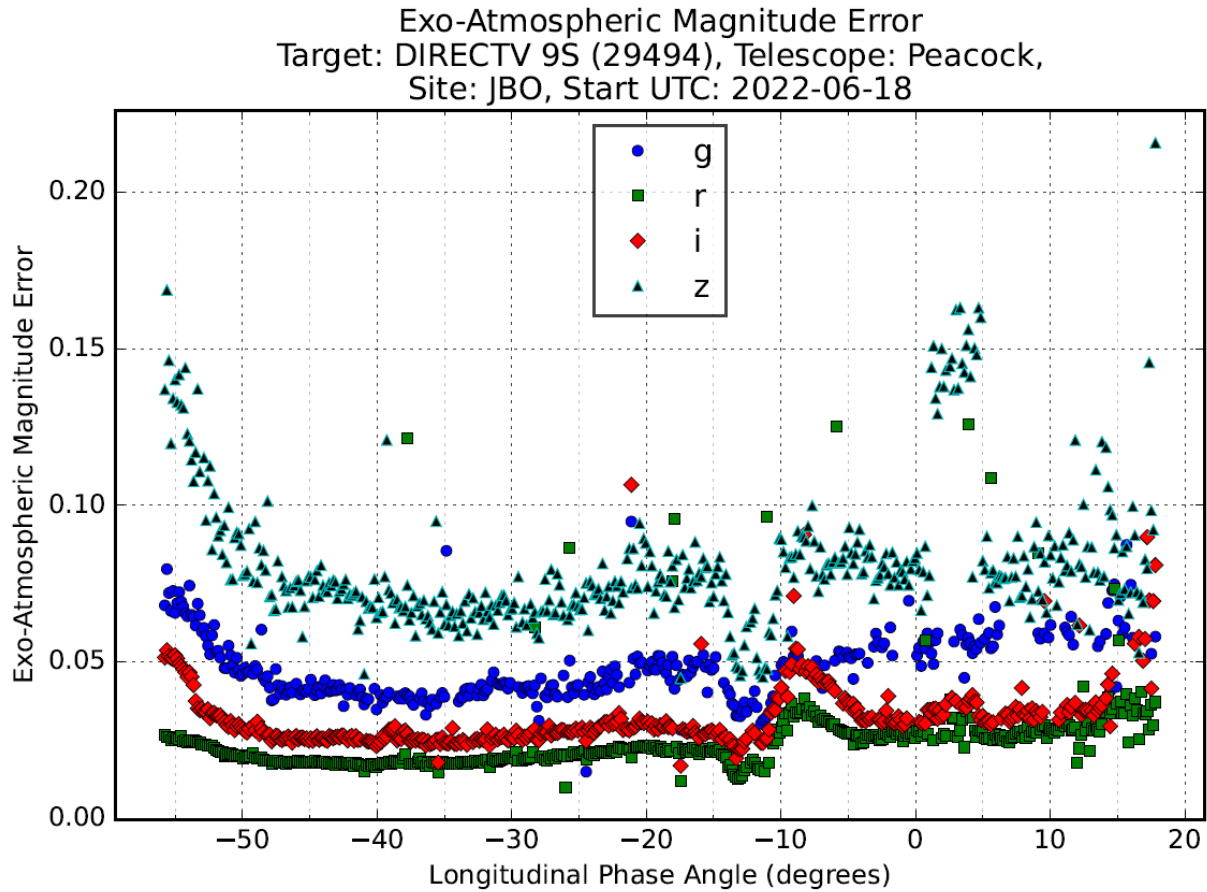


Fig. 16. Exo-atmospheric magnitude error as a function of LPA for DirecTV 9S (29494)

Similar error trends exist for SES 1 as seen in Fig. 17, although the errors in all bands are smaller and there is less difference between them. The exception is again at -8 degrees LPA when the *i*' band error is greater than the *g*' band error. Note the outlier group in *z*' band at the 0 - +5 degrees LPA range caused by the one or two bad stars in the FOV.

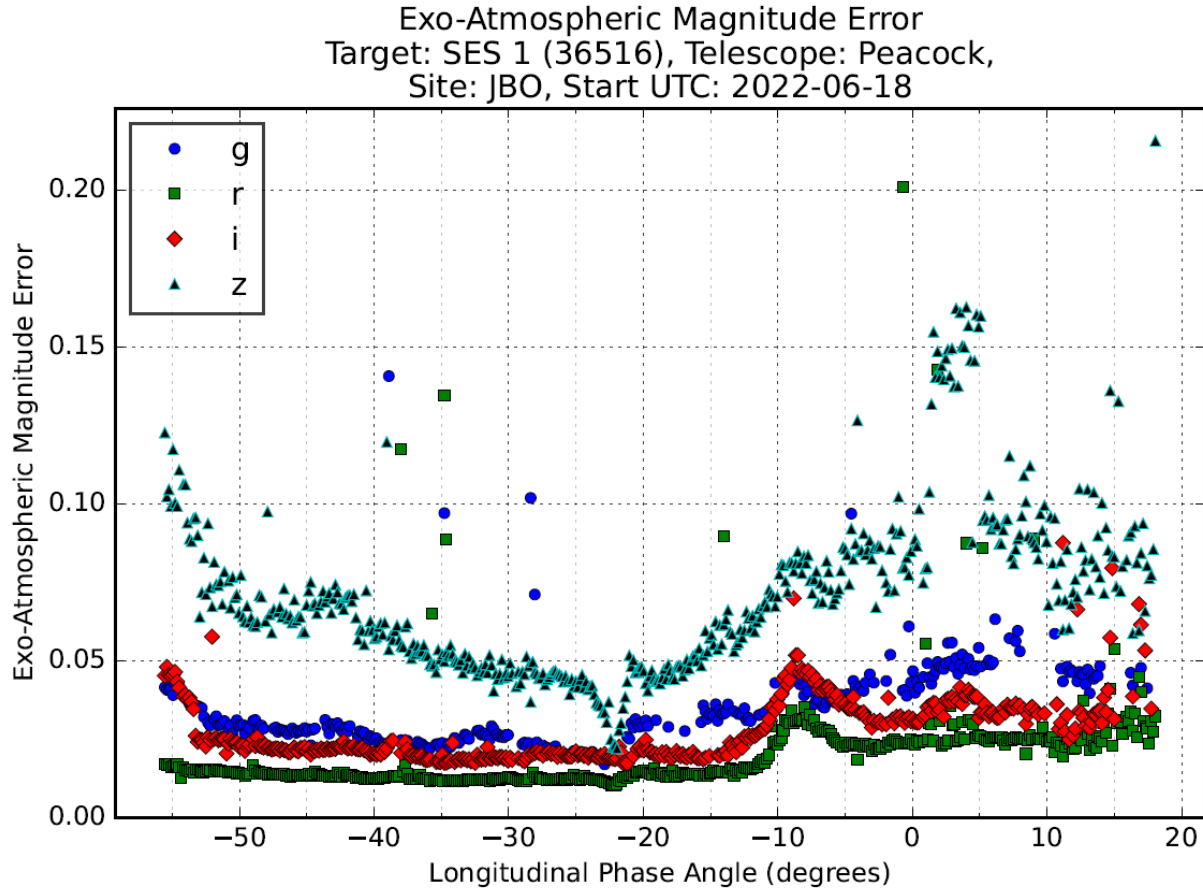


Fig. 17. Exo-atmospheric magnitude error as a function of LPA for SES 1 (36516)

The exo-atmospheric magnitude errors for AT&T T-16 are shown in Fig. 18. The satellite was overall brighter than the others and so the single exposure frames had a higher Signal-to-Noise Ratio (SNR), yielding instrumental magnitudes with higher precision. All the spectral signatures for this satellite meet our error goal except for a few spurious data points, especially at the end of the night.

It was found that the exo-atmospheric magnitude errors at -10 degrees LPA seen in all three satellites in Fig. 16–Fig. 18, which is unexpected since they are of different satellite types/configurations, were also present in the other four satellites. Note that photometric errors such as this can masquerade as intrinsic satellite features/properties. This is discussed more in Section 4.0.

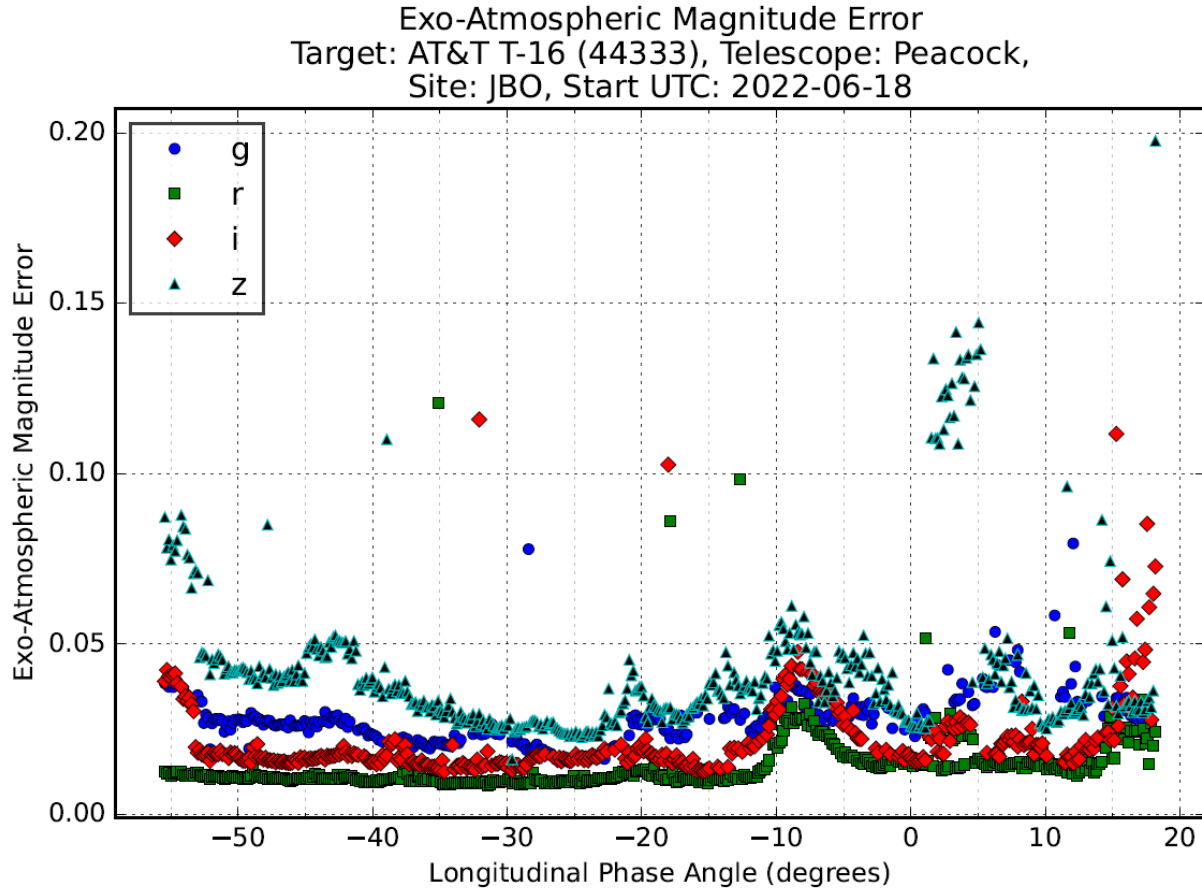


Fig. 18. Exo-atmospheric magnitude error as a function of LPA for AT&T T-16 (44333)

4.0 CONCLUSIONS AND FUTURE WORK

We have presented the initial results of the Peacock that is a persistent, multi-spectral, wide FOV system for SDA. A staring sensor has the advantage that the mount can be very simple and will not wear out from the wear and tear of slewing. A persistent sensor can maintain custody of a large number of GEOs during the entire course of the night when in-frame photometry and astrometry are employed as part of the data processing pipeline. Our implementation for simultaneous multi-spectral without sacrificing sensitivity is to replicate a COTS system for each different filter. The larger number of details from persistent multi-spectral (high cadence) signatures can be exploited to understand more details about individual satellites. We also showed that the color ranges are similar for satellites with the same bus and different for satellites constructed with different bus types, which has been shown before in [9], [10], and [11].

Currently, we sometimes meet our photometric error goal of less than 0.05 mag in exo-atmospheric magnitude error. Improvements to our image processing pipeline include implementing frame stacking to improve the SNR before performing synthetic aperture photometry to increase the instrumental magnitude precision; improving the detection and filtering out of bad stars in the frame; and adding to the quality control algorithms to increase the ability to detect star contamination. All of these improvements will ultimately decrease the exo-atmospheric magnitude errors of the Peacock data.

Finally, our initial results have illustrated how photometric errors affect the analysis of photometric signatures and highlight the importance of reporting photometric errors for each individual data point. In the case of SES 1 (and SES 3), photometric features at -10 degrees LPA could be interpreted as belonging to the satellite (Section 3.2.1)

whereas there was an effect on the photometry due to the star field that caused the photometric errors in all filters to change. Similarly, at 0 – +5 degrees LPA, all the satellites showed a cluster of outliers in the z' band caused by one or two bad stars in those frames. Without knowledge of the photometric errors for these specific data points, one might falsely conclude that some different activity was occurring on the satellite during this timeframe. These results show intriguing small-scale color changes on short timescales that deserve further study.

5.0 REFERENCES

- [1] Castro, P. and Payne, T.E., “Analysis of Induced Color Index Error Due to Sequential Filter Photometry e,” Proceedings of the Advanced Maui Optical and Space Surveillance (AMOS) Technical Conference, Sep. 27-30, 2022.
- [2] Campbell, T.S., Reddy, V., Furfaro, R., Tucker, S., “Characterizing LEO Objects using Simultaneous Multi-Color Optical Array”, Proceedings of the AMOS Technical Conference, Sep 2019.
- [3] Henden, A., Kaitchuck, R., *Astronomical Photometry*, Van Nostrand Reinhold, 1982.
- [4] Howell, S., *Handbook of CCD Astronomy*, 2nd ed., Cambridge University Press, 2006.
- [5] Payne, T.E., Mutschler, S., Shine, N., Meiser, D., Crespo, R., Beecher, E., Schmitt, L., “A Community Format for Electro-Optical Space Situational Awareness (EOSSA) Data Products”, Proceedings of the AMOS Technical Conference, Sep 2014.
- [6] Payne, T.E., Castro, P.J., Frey, V.C., Ernst, M.H., Hufford, C.R., Godar, T.J., “Enhanced Standard Data Format for Reporting Electro-Optical Data Products for Space Domain Awareness”, Proceedings of the AMOS Technical Conference, Sep 2021.
- [7] Castro, P.J., Payne, T.E., Frey, V.C., Kinader, K.K., Godar, T.J., “Calculating Photometric Uncertainty”, Proceedings of the AMOS Technical Conference, Sep 2020.
- [8] <https://space.skyrocket.de/>
- [9] Payne, T. E., Gregory, S. A., Tombasco, J., Durr, L., “Satellite Monitoring, Change Detection, and Characterization Using Non-Resolved Electro-Optical Data From a Small Aperture Telescope”, AMOS Technical Conference, September 2007.
- [10] Payne, T. E., Gregory, S. A., Hall, D.T., Wetterer, C.J., Luu, K., Vrba, F., “SSA Analysis of GEOs Photometric Signature Classifications and Solar Panel Offsets”, AMOS Technical Conference, September 2006.
- [11] Payne, T. E., Gregory, S. A., Vrba, F. J., Luu, K., “Utility of a Multi-Color Photometric Database”, AMOS Technical Conference, Wailea, HI, September 2005.

ACKNOWLEDGEMENTS

The authors would like to express their gratitude to Dr. Anil B. Chaudhary (Applied Optimization Inc.) for his financial and moral support of this internal R&D project. We also want to acknowledge Dr. David Monet (AFRL/RVSW) for bringing his concept for this type of system to Applied Optimization and working with us to identify the COTS technology to implement a persistent, simultaneous, multi-spectral, wide-field-of-view system for SDA.